

Journal of Materials Chemistry A

Accepted Manuscript



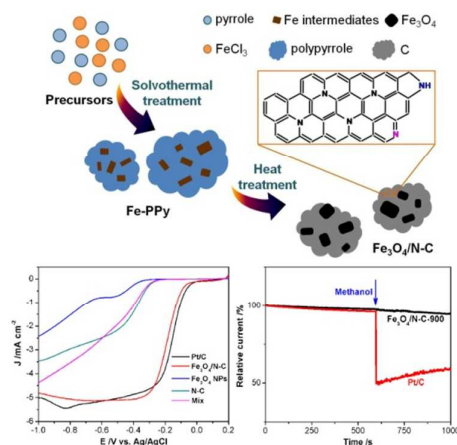
This is an *Accepted Manuscript*, which has been through the Royal Society of Chemistry peer review process and has been accepted for publication.

Accepted Manuscripts are published online shortly after acceptance, before technical editing, formatting and proof reading. Using this free service, authors can make their results available to the community, in citable form, before we publish the edited article. We will replace this *Accepted Manuscript* with the edited and formatted *Advance Article* as soon as it is available.

You can find more information about *Accepted Manuscripts* in the [Information for Authors](#).

Please note that technical editing may introduce minor changes to the text and/or graphics, which may alter content. The journal's standard [Terms & Conditions](#) and the [Ethical guidelines](#) still apply. In no event shall the Royal Society of Chemistry be held responsible for any errors or omissions in this *Accepted Manuscript* or any consequences arising from the use of any information it contains.

Graphical Abstract



Via a solvothermal carbonization process, an enriched graphitic N-doped carbon-supported Fe₃O₄ nanoparticles composite was prepared. The hybrid composite exhibits similar high catalytic activity but superior stability to Pt/C for ORR. The unusual high catalytic activity arises from the combination of the high surface area and the synergetic coupling effect between the enriched graphitic N-doped carbon and Fe₃O₄ nanoparticles.

Cite this: DOI: 10.1039/c0xx00000x

www.rsc.org/xxxxxx

ARTICLE TYPE

Enriched graphitic N-doped carbon-supported Fe₃O₄ nanoparticles as efficient electrocatalysts for oxygen reduction reaction

Yunhe Su,^{a,b} Hongliang Jiang,^a Yihua Zhu,^{*a} Xiaoling Yang,^a Jianhua Shen,^a Wenjian Zou,^a Jianding Chen,^{*b} and Chunzhong Li^a

Received (in XXX, XXX) XthXXXXXXXXXX 20XX, Accepted Xth XXXXXXXXXXXX 20XX

DOI: 10.1039/b000000x

Graphitic N is proposed to be one of the most likely active sites for oxygen reduction reaction (ORR) in N-doped carbon materials. However, the recent hybrid composites consisting of N-doped carbons and transition metal oxides for ORR are predominantly pyridinic N- and pyrrolic N-doped carbons-supported cobalt or manganese oxides. Here, an enriched graphitic N-doped carbon-supported Fe₃O₄ nanoparticles composite was prepared via a solvothermal carbonization process. The hybrid composite exhibits similar high catalytic activity with 4e⁻ reaction pathway but superior stability to Pt/C for ORR in alkaline media. Furthermore, the composite also shows better ORR performance than previously reported transition metal oxides based N-doped carbon hybrid composites. The unusual high catalytic activity arises from the combination of the high surface area and the synergetic coupling effect between the enriched graphitic N-doped carbon and Fe₃O₄ nanoparticles.

Introduction

Catalysts for oxygen reduction reaction (ORR) are at the heart of renewable-energy applications such as fuel cells and metal-air batteries.¹ Pt and its alloys have long been regarded as the most efficient catalysts for ORR, however, high cost, limited supply and poor stability severely prevent them from being a sustainable solution to ORR. Therefore, Pt-free catalysts with high ORR activity, low cost and superior stability have been actively pursued.^{2,3}

Currently, N-doped carbon materials are considered to be a potential substitute for Pt to reduce the cost and enhance the stability of ORR catalysts.⁴⁻⁶ The incorporation of N element into carbon materials endows them unique electronic properties due to the conjugation between the N lone-pair electrons and the graphene π system, and thus significantly enhance the number of active sites for ORR.^{7,8} It is proposed that the inherent active sites for ORR in N-doped carbon materials might include pyridinic, pyrrolic, and graphitic N species. Among them, graphitic N is regarded as one of the most likely ORR active sites because the graphitic N atoms in the carbon lattice facilitate electron transfer from the carbon electronic bands to the anti-bonding orbitals of O₂.⁹⁻¹¹ Although great efforts have been done to synthesize various N-doped carbon materials, their ORR activities are still on a less competitive level compared to Pt-based catalysts. Hence, it is still important to develop new strategy to further improve the ORR activities of N-doped carbon materials.

In the past decades, transition metal oxides (Co₃O₄, MnO₂, etc.) have also been widely studied as alternative ORR catalysts in alkaline solution because of their low cost, abundance and

environmental compatibility.¹²⁻¹⁴ Nevertheless, pristine transition metal oxides usually exhibit limited ORR activities probably due to their low electrical conductivity. Loading of transition metal oxides on conducting carbon supports can overcome this limitation and improve the ORR activity.¹⁵⁻¹⁷ In this way, considering that both N-doped carbon materials and transition metal oxides have considerable ORR activities, it will be attractive to study the ORR performances of their hybrid composites. Just recently, some hybrid catalysts based on N-doped carbon materials and transition metal oxides have been reported to exhibit enhanced ORR activity and superior stability.¹⁸⁻²⁰ However, in those studies, as far as we know, due to the higher formation energy of graphitic N dopant and the relatively mild synthesis methods, the doped N species in the N-doped carbon materials are predominantly pyridinic and pyrrolic N, which could be less active owing to the lack of graphitic N.^{5,9,21} Furthermore, most of those studies are devoted to cobalt and manganese oxides based N-doped carbon materials, and few has been carried out in regard to Fe₃O₄ based N-doped carbon materials, presumably due to the low ORR activity of pristine Fe₃O₄ nanoparticles or mixture with N-doped carbons. Therefore, it is encouraging and interesting to investigate the ORR performance of hybrid composite consisting of graphitic N-doped carbon and Fe₃O₄ nanoparticles.

Experimental

Instrumentation and Chemicals.

Electrochemical experiments were conducted on a CHI660C electrochemical workstation (CH Instrument Co., China). A conventional three-electrode system included a glassy carbon

rotating disk electrode (RDE) (5 mm in diameter, Pine Research Instrumentation) coated with catalysts, a Pt wire counter electrode and an Ag/AgCl (KCl, 3.5 M) reference electrode. Transmission electron microscopy (TEM) studies were performed on a JEM-2100 high-resolution transmission electron microscope equipped with an energy dispersive X-ray analyzer (EDX). The samples were placed on a carbon-coated copper grid and dried at room temperature overnight. X-ray diffraction (XRD) patterns were collected on a powder X-ray diffractometer (RIGAKU, D/MAX 2550 VB/PC, Japan) Scanning electron microscopy (SEM) images were recorded on the S-4800 field emission scanning electron microscope at high vacuum with an accelerating voltage of 10 kV. Raman spectra were collected on a Bruker RFS 100/S spectrometer with 514 nm laser excitation and Fourier transform infrared (FTIR) spectra were performed with the transmission module of Thermo Nicolet 5700 FTIR spectrometer. Thermogravimetric analysis (TGA) of sample was performed on a SDT-Q600 simultaneous TGA/DSC thermogravimetric analyzer (TA Instruments), and the sample was heated under air atmosphere from room temperature to 800 °C at 10 °C min⁻¹. X-ray photoelectron spectroscopy (XPS) was conducted using a VG ESCA 2000 with an Mg K α as the source and using the C 1s peak at 284.6 eV as an internal standard. Brunauer–Emmett–Teller (BET) and Barrett–Joyner–Halenda (BJH) models were used to determine the specific surface areas, pore volume, and pore sizes of the samples, respectively. All chemicals were of analytical grade and used without further purification. Ultrapure water ($\geq 18\text{M}\Omega\text{ cm}^{-1}$) was used throughout.

Materials Synthesis.

Synthesis of Fe₃O₄/N-C composites: Ferric chloride (0.811 g, 3.0 mmol) was first dissolved in anhydrous ethanol (30 mL), and then mixed with the anhydrous ethanol (30 mL) solution of pyrrole (0.201 g, 3.0 mmol) under continuous stirring for about 30 min. The resulting solution was sealed in a 100 mL Teflon-lined autoclave and solvothermally treated at 180 °C for 12 h, followed by natural cooling to room temperature. The precipitates were collected by centrifugation, washed with ultrapure water and anhydrous ethanol for three times, and finally dried at 60 °C overnight. After that, the as-prepared samples were pyrolyzed at 800–1100 °C for 4 h under flowing argon gas.

Synthesis of N-doped carbon: Ammonium persulfate (0.684 g, 3.0 mmol) was first dissolved in ultrapure water (30 mL), and then mixed with the anhydrous ethanol (30 mL) solution of pyrrole (0.201 g, 3.0 mmol) under continuous stirring for about 30 min. The resulting solution was sealed in a 100 mL Teflon-lined autoclave and solvothermally treated at 180 °C for 12 h, followed by natural cooling to room temperature. The precipitates were collected by centrifugation, washed with ultrapure water and anhydrous ethanol, and finally dried at 60 °C overnight. After that, the as-prepared samples were pyrolyzed at 900 °C for 4 h under flowing argon gas.

Synthesis of Fe₃O₄ nanoparticles: Pristine Fe₃O₄ nanoparticles were synthesized following a reported methodology.²² Briefly, Ferric chloride (0.811 g, 3.0 mmol), Sodium acetate (2.04 g, 15.0 mmol), and sodium dodecyl sulfate (1.090 g, 4.0 mmol) and polyethylene glycol (0.4 g, ~7 mmol) were added to ethylene glycol (24.0 ml) to form colloid mixture under vigorous stirring

at room temperature. Then, the mixture was sealed in a teflon-lined stainless-steel autoclave of 50 ml capacity. Finally, the autoclave was heated and maintained at 180 °C for 72 h, and allowed to cool down to room temperature naturally. The black products were washed several times with absolute ethanol and dried at 60 °C for 6 h.

Electrode preparation and Electrochemical Tests.

The RDEs were polished with 1 and 0.05 μm alumina slurry sequentially and then washed ultrasonically in ultrapure water and ethanol, respectively. The catalysts (3 mg) were ultrasonically dispersed in the mixed solution of Nafion (5 wt%, 100 μL) and ethanol (900 μL), resulting in a catalyst concentration of 3 mg mL⁻¹. Then the catalyst dispersion (10 μL) was dropped onto the RDE, which yielded a loading of catalyst 0.15 mg cm⁻². The resulting electrode was dried under ambient conditions. All electrochemical tests, including cyclic voltammograms (CVs), linear sweep voltammetry (LSVs) and chronoamperometry, were performed at room temperature in 0.1 M KOH solutions, which were purged with N₂ or O₂ for at least 30 min prior to each measurement. Tests for CVs and LSVs were scanned between -1.0 and +0.2 V at 10 mV s⁻¹, and LSVs were recorded at various rotating speeds from 400 to 1600 rpm. Chronoamperometry tests were conducted in O₂-saturated 0.1 M KOH at -0.4 V with a rotation rate of 900 rpm. The exact kinetic parameters, including electron transfer number (n) and kinetic current density (J_k) involved in the typical ORR process were analyzed based on the Koutecky-Levich (K-L) equation:^{1,23}

$$\frac{1}{J} = \frac{1}{J_L} + \frac{1}{J_K} = \frac{1}{B\omega^{1/2}} + \frac{1}{J_K}$$

$$B = 0.2nFC_0(D_0)^{2/3}\nu^{-1/6}$$

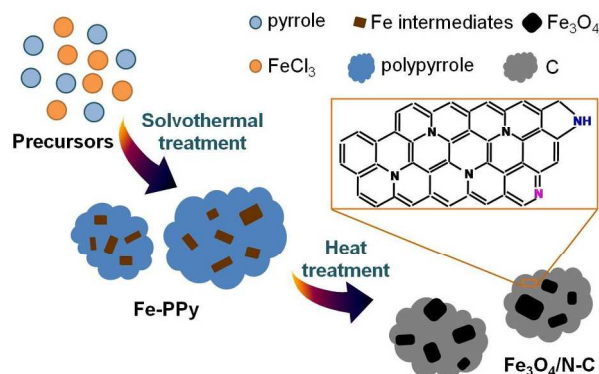
In the Koutecky-Levich equation, J , J_L , J_k are the measured current density, the diffusion current density, and the kinetic current density, respectively; ω is the rotation speed in rpm, F is the Faraday constant (96485 C mol⁻¹), D_0 is the diffusion coefficient of oxygen in 0.1 M KOH (1.9×10^{-5} cm² s⁻¹), ν is the kinetic viscosity (0.01 cm² s⁻¹), and C_0 is the bulk concentration of oxygen (1.2×10^{-6} mol cm⁻³). The constant 0.2 is adopted when the rotating speed is expressed in rpm.

Results and discussion

In this work, we describe a solvothermal carbonization method to in situ prepare enriched graphitic N-doped carbon supported Fe₃O₄ nanoparticles (Fe₃O₄/N-C). The as-prepared Fe₃O₄/N-C-900 composite shows greatly enhanced catalytic activity and excellent stability towards ORR in alkaline solution. The fabrication process of Fe₃O₄/N-C using pyrrole and FeCl₃ as precursors is illustrated in Scheme 1 together with the predicted microstructure of the N-doped carbon in Fe₃O₄/N-C, further details of synthesis can be found in the Experimental Section. Here, FeCl₃ is used not only as an oxidant for pyrrole polymerization, but also as reactant for the formation of Fe-containing intermediates. Meanwhile, owing to the good solubility of pyrrole and FeCl₃ in ethanol solvent, Fe

intermediates could be uniformly formed and well embedded into polypyrrole during the solvothermal treatment. Moreover, in the pyrolysis step, the as-prepared Fe-containing intermediates-doped polypyrrole (Fe-PPy) is employed as the only pyrolytic precursor providing nitrogen, carbon and iron, which substantially reduces the precursor number and simplifies the procedure.

To study the effect of the pyrolysis temperature on the catalytic activity of Fe₃O₄/N-C, linear-sweep voltammograms at 1600 rpm were collected in O₂-saturated 0.1 M KOH for Fe₃O₄/N-C samples carbonized under different temperatures (Supporting Information, Figure S1). The activity increased with increasing treatment temperature from 800 °C to 900 °C, but decreased when the temperature increased to 1100 °C. We selected 900 °C as optimal treatment temperature, and thus chose the Fe₃O₄/N-C-900 catalyst for more detailed studies.



Scheme 1. Illustration of the fabrication process for Fe₃O₄/N-C, and the possible microstructures of the N-doped carbon in Fe₃O₄/N-C.

X-ray diffraction (XRD) was used to obtain structural information about Fe₃O₄/N-C-900. Fig. 1a shows X-ray diffraction patterns of Fe₃O₄/N-C-900. The well-defined peaks at around 30°, 35.5°, 43°, 53.5°, 57°, 63° are in good agreement with the Joint Committee on Powder Diffraction Standards (JCPDS) card 39-1346, which confirms the formation of Fe₃O₄. The relatively sharp diffraction peaks at around 2θ=25° and 43°, corresponding to C (002) and (101) diffractions, indicating the partially graphitized structure of the N-doped carbon in Fe₃O₄/N-C-900. Notably, in the XRD patterns of Fe-PPy, only a broad C (002) diffraction peak can be obviously identified and observed, which suggests that the Fe-containing intermediates might be amorphous phase (Supporting Information, Figure S2). This speculation could further be supported by the step scanning XRD measurement of Fe-PPy at a very slow scan rate of 1 °C/min from 20 to 40 degree, as presented in Figure S3.

Scanning electron microscopy (SEM) image reveals a granular-like morphology of Fe₃O₄/N-C-900 (Fig. 1b), which demonstrates a similar but shrunken sized morphology of Fe-PPy owing to the carbonization process (Supporting Information, Figure S4). Transmission electron microscopy (TEM) images in Fig. 1c and Figure S5a suggest that the Fe₃O₄ nanoparticles incorporated in the carbon layers mainly exhibit a size range of 30-150 nm, while from the corresponding dark-field TEM image (Figure S5b), a lot of small sized bright dots could also be identified and observed, which suggests that a large number of small sized Fe₃O₄ nanoparticles (<20 nm) are existed in the carbon layers. The inset in Fig. 1c shows the selected area

electron diffraction (SAED) pattern, implying a polycrystalline crystal structure of Fe₃O₄ nanoparticles. The SAED pattern is less clear because the content of Fe₃O₄ in the Fe₃O₄/N-C-900 composite is too low, which results in a weak diffraction intensity. Short-range ordered, graphitized carbons can be observed from the high-resolution TEM (HRTEM) image (Fig. 1d), and the inset shows a small sized Fe₃O₄ aggregates surrounded by the graphitized carbons. It has been reported previously that the interactions between transition metal oxides and N-doped carbon materials can lead to improved ORR activity.^{1, 2, 18, 20} Then it is predictable that a similar mechanism may also work in our Fe₃O₄/N-C hybrid system due to the interaction between the small sized Fe₃O₄ nanoparticles and the N-doped graphitized carbon. Through TEM and the energy dispersive X-ray (EDX) spectroscopy characterizations of Fe-PPy, the existence of Fe-containing intermediates could also be proved (Supporting Information, Figure S6 and Figure S7). It is notable that some Cl atoms existed in the Fe-containing intermediates-doped polypyrrole (Fe-PPy) which we have washed sufficiently. We think that this might be caused by two reasons: (i) During the solvothermal treatment process, Cl ions may be incorporated into the polypyrrole matrix and generate Cl anions-doped polypyrrole due to the abundant FeCl₃ reactant;²⁴⁻²⁶ (ii) Owing to the uncertainty of Fe-containing intermediates, it may contain Cl atoms in the Fe-containing intermediates, which causes the presence of Cl in the resulting Fe-PPy.

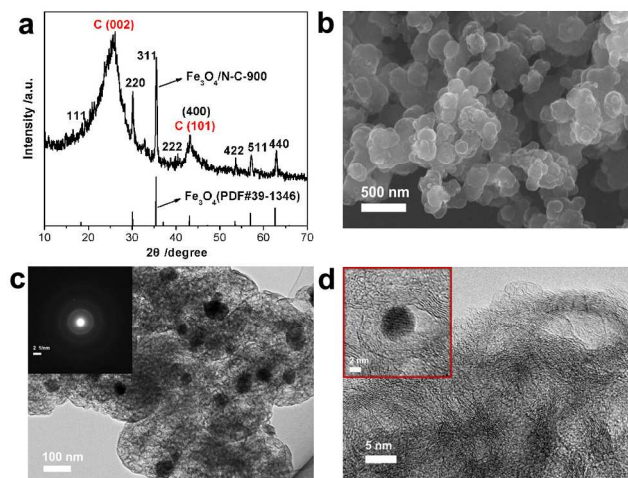


Fig. 1 (a) XRD patterns of Fe₃O₄/N-C-900; (b) SEM and (c) TEM images of Fe₃O₄/N-C-900, inset of (c) shows the corresponding SAED pattern; (d) HRTEM images of Fe₃O₄/N-C-900, inset shows the small sized Fe₃O₄ aggregates surrounded by graphitized carbon.

The carbon structure of Fe₃O₄/N-C-900 was analyzed by Raman spectra (Fig. 2a). The D-band at 1346 cm⁻¹ arises from the disorder in sp² hybridized carbon, and the G-band at 1575 cm⁻¹ corresponds to graphitic structures. The broad bands centered at 2680 cm⁻¹ and 2900 cm⁻¹ are ascribed to the 2D and D+G bands. The high I_G/I_D ratio (1.06) indicates the partial graphitization of carbons in Fe₃O₄/N-C-900, which agrees with the XRD and HRTEM results.²⁷ Moreover, a weak Raman signal at about 660 cm⁻¹ was observed, which could be attributed to the A_{1g} mode of Fe₃O₄.²⁸ The porous nature of Fe₃O₄/N-C-900 was accessed with nitrogen adsorption-desorption isotherms (Fig. 2b). The isotherm of Fe₃O₄/N-C-900 can be classified as a type-IV isotherm with a

high BET surface area of $210.6 \text{ m}^2 \text{ g}^{-1}$. The distinct hysteresis loop in the large range of ca. 0.2-0.8 P/P_0 indicates the presence of mesoporous structure.^{2, 29, 30} The pore size distribution calculated from desorption data using the BJH model, suggests an average value of 3.87 nm. It is obvious that the high specific surface area is mainly attributed to the mesoporous structure. The high surface area of $\text{Fe}_3\text{O}_4/\text{N-C-900}$ could provide higher surface density of catalytic active sites exposed to oxygen molecules and the mesoporous structure could also provide the possibility of efficient mass transport, which lead to enhanced catalytic activity.^{30, 31}

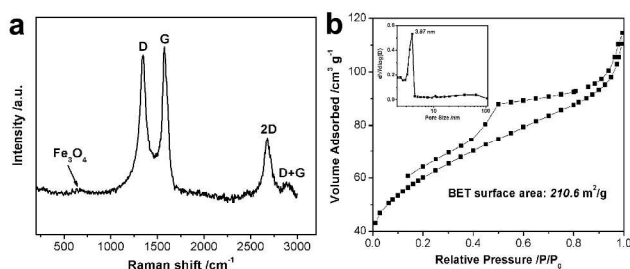


Fig. 2 (a) Raman spectra and (b) Nitrogen adsorption and desorption isotherm of $\text{Fe}_3\text{O}_4/\text{N-C-900}$, inset of (b) shows the BJH pore distribution.

X-ray photoelectron spectroscopy (XPS) was used to characterize the elemental composition of $\text{Fe}_3\text{O}_4/\text{N-C-900}$. As shown in Fig. 3a, four predominant peaks, corresponding to the C1s, O1s, N1s and Fe2p, are visible at about 284.6 eV, 532 eV, 401 eV and 711 eV, respectively. The deconvolution of C1s spectrum showed that there was 68.6% C=C, 14.3% C=N & C-O, 10.1% C-N & C=O, and 7.0% O-C=O, indicating the existence of carbon atoms connected to N and O heteroatoms (Fig. 3b). The high-resolution N1s could be deconvoluted into four types of N species and the graphitic N dominates the majority: 14.2% pyridinic N, 3.5% pyrrolic N, 78.0% graphitic N, and 4.3% oxidized N (Fig. 3c). These results clearly demonstrate the successful incorporation of nitrogen atoms into the carbon framework. A schematic structure of N-doped carbon showing the bonding configurations of N atoms is given in the supporting information (Supporting Information, Scheme S1). It has been demonstrated that graphitic N could greatly increase the limiting current density, and pyridinic N could improve the onset potential, while other N species such as pyrrolic N or oxidized N had little effect on the electrochemical performance of carbon materials.⁹ Furthermore, some previous work have reported that a larger amount of graphitic N than pyridinic N is considered to be favourable for ORR.^{32, 33} Thus, the enriched graphitic N-doped carbon in this work might have a positive effect on the ORR activity of $\text{Fe}_3\text{O}_4/\text{N-C-900}$. The Fe2p spectrum shows typical peaks of Fe2p 1/2 and Fe2p 3/2 of oxidized Fe species, which can be deconvoluted into five peaks at 710.9, 713.6, 718.7, 723.0 and 725.2 eV (Fig. 3d). These are consistent with the previous report and further verify the existence of Fe_3O_4 .³⁴⁻³⁶ The photoelectron peaks at 725.2 eV is attributed to the binding energies of 2p 1/2 of Fe(III) and Fe(II) ions, the peaks at 722.9 eV can be assigned to the binding energies of 2p 1/2 of Fe(II) ion.^{37, 38} The peak at 713.6 and 710.7 eV can be assigned to the 2p 3/2 of Fe(III) ion and Fe(II) ion, respectively.³⁹ The peak at 718.7 eV is a satellite peak for the above four peaks, indicating the co-existing of Fe(III) and Fe(II) in the catalyst. Moreover, the high-resolution

O1s spectrum could be fitted into four peaks at 533.1, 532.0, 530.7 and 530.2 eV, which corresponds to hydroxyls, carboxyls, physically adsorbed oxygen/carbonates and the oxygen related to Fe_3O_4 , respectively (Fig. 3e).⁴⁰ Interestingly, thermogravimetric (TG) analysis reveals that the mass fraction of Fe_3O_4 in $\text{Fe}_3\text{O}_4/\text{N-C-900}$ is about 14 wt% (Fig. 3f), which is much higher than that calculated from XPS (ca. 5 wt% converted from the 0.8 at% of Fe (Supporting Information, Table S1)). This is because XPS analysis is more sensitive to the surface chemical composition (ca. 5 nm), which could hardly detect the Fe_3O_4 nanoparticles incorporated in carbon nanosheets (Fig. 1c).⁴¹

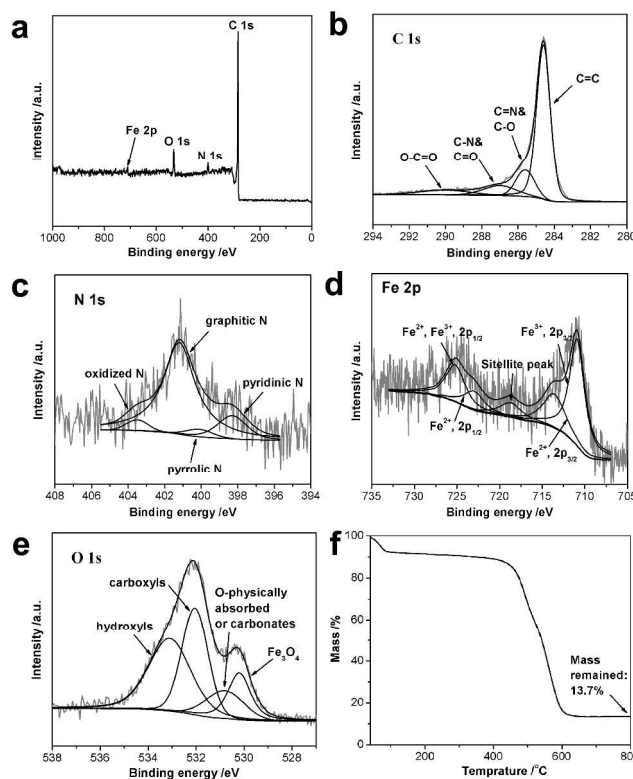


Fig. 3 (a) XPS spectra of $\text{Fe}_3\text{O}_4/\text{N-C-900}$; high-resolution (b) C 1s, (c) N 1s, (d) Fe 2p and (e) O 1s spectra; (f) TG analysis of $\text{Fe}_3\text{O}_4/\text{N-C-900}$.

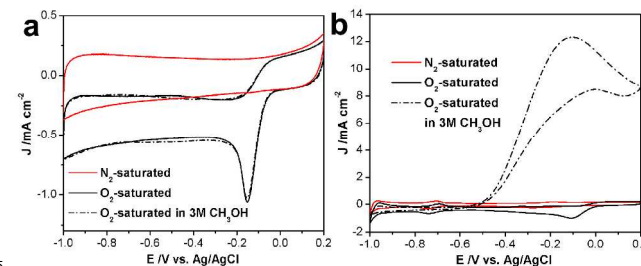


Fig. 4 CVs in N_2 - and O_2 -saturated 0.1 M KOH, in an O_2 -saturated 0.1 M KOH upon the addition of CH_3OH (3 M) for (a) $\text{Fe}_3\text{O}_4/\text{N-C-900}$ and (b) Pt/C.

The ORR catalytic activity of $\text{Fe}_3\text{O}_4/\text{N-C-900}$ was initially investigated using cyclic voltammogram (CV) measurements in 0.1 M KOH at a scan rate of 10 mV s^{-1} . Featureless voltammetric currents within the potential range between -1.0 and +0.2 V are observed for $\text{Fe}_3\text{O}_4/\text{N-C-900}$ in N_2 -saturated solution, while the reduction current appears as a well-defined cathodic peak at -0.15 V in O_2 -saturated 0.1 M KOH solution, suggesting pronounced

electrocatalytic activity of $\text{Fe}_3\text{O}_4/\text{N-C-900}$ for ORR (Fig. 4a). Furthermore, we measured the catalytic selectivity of $\text{Fe}_3\text{O}_4/\text{N-C-900}$ and Pt/C against the electrooxidation of methanol in O_2 -saturated 0.1 M KOH in the presence of methanol (3.0 M). The Pt/C shows a distinct response corresponding to methanol oxidation, whereas the cathodic peak for ORR disappears (Fig. 4b). In contrast, no noticeable change was observed for $\text{Fe}_3\text{O}_4/\text{N-C-900}$ under the same condition, indicating excellent selectivity of $\text{Fe}_3\text{O}_4/\text{N-C-900}$ compared to Pt/C (Fig. 4a). Notably, this result could also be verified by the time-current responses of $\text{Fe}_3\text{O}_4/\text{N-C-900}$ and Pt/C in O_2 -saturated 0.1 M KOH with the adding of methanol (Fig. 6a).

To better compare and understand the ORR performance of $\text{Fe}_3\text{O}_4/\text{N-C-900}$ composite, N-doped carbon (N-C) and pristine Fe_3O_4 nanoparticles (Fe_3O_4 NPs) were also prepared and used as control catalysts. Linear sweep voltammetry (LSV) measurements for $\text{Fe}_3\text{O}_4/\text{N-C-900}$, N-C, Fe_3O_4 NPs, physical mixture of N-C and Fe_3O_4 NPs (Mix), and commercial Pt/C (20 wt% Pt) were performed on a rotating-disk electrode (RDE) in O_2 -saturated 0.1 M KOH at a rotation rate of 1600 rpm. As shown in Fig. 5a, the $\text{Fe}_3\text{O}_4/\text{N-C-900}$ presents a positive onset potential of -0.055 V and a current density of 5.12 mA cm^{-2} at -0.6 V, very close to those of Pt/C (-0.024 V and 5.14 mA cm^{-2}), and much higher than those of Fe_3O_4 NPs (-0.356 V and 0.78 mA cm^{-2}), N-C (-0.266 V and 2.49 mA cm^{-2}) and Mix (-0.272 V and 2.52 mA cm^{-2}). The more positive onset potential and larger current density of $\text{Fe}_3\text{O}_4/\text{N-C-900}$ than those of Fe_3O_4 NPs, N-C and Mix should also suggest the existence of synergetic effect between Fe_3O_4 and N-C in the composite. Furthermore, the as-prepared $\text{Fe}_3\text{O}_4/\text{N-C-900}$ here exhibits better ORR performance than previously reported transition metal oxides based N-doped carbon hybrid materials, indicating a highly efficient ORR catalyst of $\text{Fe}_3\text{O}_4/\text{N-C-900}$ in alkaline solution (Table 1). We speculate that the high ORR activity of $\text{Fe}_3\text{O}_4/\text{N-C-900}$ could be attributed to the combination of the high surface area of $\text{Fe}_3\text{O}_4/\text{N-C-900}$ and the synergetic effect between the enriched graphitic N-doped carbons and Fe_3O_4 nanoparticles.

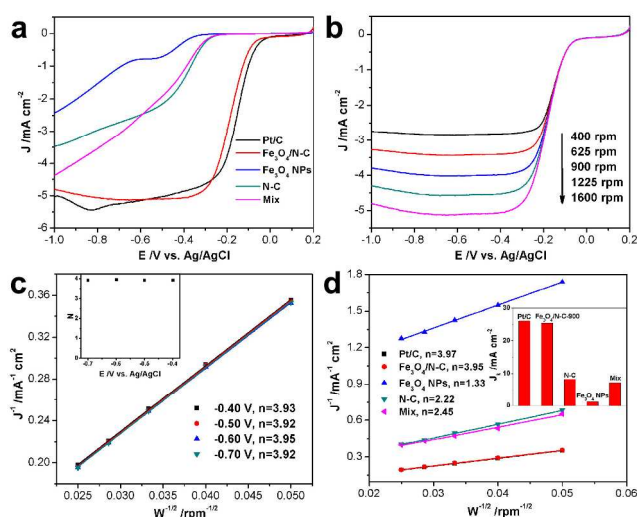


Fig. 5 (a) LSVs for $\text{Fe}_3\text{O}_4/\text{N-C-900}$, N-C, Fe_3O_4 NPs, Mix and Pt/C; (b) LSVs at different rotating speeds and (c) K-L plots for $\text{Fe}_3\text{O}_4/\text{N-C-900}$, inset of (d) shows the electron transfer number at different potentials; (d) K-L plots at -0.6 V for $\text{Fe}_3\text{O}_4/\text{N-C-900}$, N-C, Fe_3O_4 NPs, Mix and Pt/C,

inset show the corresponding J_k values; (f) I-t plots of $\text{Fe}_3\text{O}_4/\text{N-C-900}$ and Pt/C at -0.4 V.

Typical LSVs of $\text{Fe}_3\text{O}_4/\text{N-C-900}$ at various rotating speeds were recorded in Fig. 5b. The voltammetric profiles in O_2 -saturated 0.1 M KOH electrolyte show that the current density was enhanced with increasing rotation rates (from 400 to 1600 rpm). Fig. 5c shows the Koutecky-Levich plots (J^{-1} vs $W^{-1/2}$) at different potentials for $\text{Fe}_3\text{O}_4/\text{N-C-900}$, the linearity of the Koutecky-Levich plots and near parallelism of the fitting lines suggests first-order reaction kinetics toward the concentration of dissolved oxygen and similar electron transfer number for ORR at different potentials.^{1, 2, 29} The inset of Fig. 5c demonstrates that the electron transfer number of $\text{Fe}_3\text{O}_4/\text{N-C-900}$ remains approximately constant at 3.92 over the potential range from -0.40 to -0.70 V, emphasizing the ORR proceeds via a four-electron mechanism. Fig. 5d showed the Koutecky-Levich plots for $\text{Fe}_3\text{O}_4/\text{N-C-900}$, N-C, Fe_3O_4 NPs, Mix and Pt/C at -0.60 V, the corresponding kinetic current density (J_k) calculated based on the Koutecky-Levich equation were also depicted in the inset of Fig. 5d. The higher electron transfer number and J_k of $\text{Fe}_3\text{O}_4/\text{N-C-900}$ than those of Fe_3O_4 NPs, N-C and Mix further manifest that a synergetic promotion of ORR performance arises from the enriched graphitic N-doped carbon supported Fe_3O_4 nanoparticles composite.

Table 1. A benchmark of our $\text{Fe}_3\text{O}_4/\text{N-C-900}$ with values obtained from some other independent literatures. All in alkaline condition with KOH 0.1 M.

Materials	Technique	Loading (mg/cm ²)	Activity (V vs. Ag/AgCl) ^[a]	Refs.
$\text{Fe}_3\text{O}_4/\text{N-C-900}$	CV, LSV	0.15	$E_p = -0.15$ $E_{\text{onset}} = -0.055$ $E_{1/2} = -0.184$ $E_{1/2} = -0.199$	In this work ^[b]
$\text{Co}_3\text{O}_4/\text{N-graphene}$	LSV	0.17	$E_p = -0.21$ $E_{1/2} = -0.219$	1
MnO/m-N-C	CV, LSV	0.10	$E_p = -0.21$ $E_{1/2} = -0.219$	2
CoO/N-CNT	CV, LSV	0.10	$E_{\text{onset}} = -0.099$ $E_p = -0.169$	18
$\text{Fe}_3\text{O}_4/\text{N-GAs}$	LSV	0.14	$E_{\text{onset}} = -0.19$	19
$\text{Mn}_3\text{O}_4/\text{N-graphene}$	CV, LSV	0.20	$E_p = -0.3$ $E_{\text{onset}} = -0.09$	20

^[a] All the potential values from references were converted to vs. Ag/AgCl for comparison.

^[b] In order to minimize the effect of residual currents on the potential value, the onset potential in this research has been defined as a potential required for generating an ORR current density of 0.1 mA cm^{-2} in the LSV experiment.

The methanol crossover effect was evaluated using chronoamperometric measurements at -0.4 V in O_2 -saturated 0.1 M KOH with a rotation rate of 900 rpm with the addition of 3.0 M methanol (Fig. 6a). A significant drop in current appeared at the Pt/C electrode upon the addition of 3.0 M methanol. In contrast, no noticeable change was observed in the ORR current at the $\text{Fe}_3\text{O}_4/\text{N-C-900}$ electrode. This suggests that the $\text{Fe}_3\text{O}_4/\text{N-C-900}$ electrode has a higher ORR selectivity and greater tolerance to methanol crossover than the commercial Pt/C catalyst, which agrees with the CV results in Figure 4. Additionally, chronoamperometric durability tests for the ORR

were also performed (Fig. 6b).^{2, 41-43} The Pt/C catalyst shows a 16.4% decrease in activity after 10000 s at -0.4 V. As a comparison, Fe₃O₄/N-C-900 retains a high relative current of 90.4% after 10000 s, indicating a superior stability of active reaction sites on Fe₃O₄/N-C-900 than that on commercial Pt/C in alkaline environment.

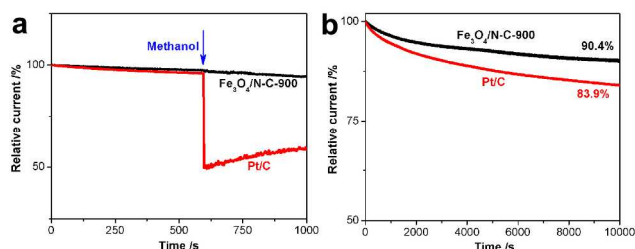


Fig. 6 I-t plots of Fe₃O₄/N-C-900 and Pt/C at -0.4 V in O₂-saturated 0.1 M KOH (a) with and (b) without the adding of methanol (1.0 M).

Conclusions

In summary, via a solvothermal carbonization approach, a novel non-precious ORR catalyst of enriched graphitic N-doped carbon supported Fe₃O₄ nanoparticles has been reported. Because of the high surface area and synergistic effect between the enriched graphitic N-doped carbon and Fe₃O₄ nanoparticles, the resulting Fe₃O₄/N-C composite shows comparable high catalytic activity and superior stability to the commercial Pt/C catalyst for ORR. It is anticipated that the Fe₃O₄/N-C used as an ORR catalyst in alkaline fuel cell would offer a competitive advantage over state-of-the-art Pt/C catalysts.

Acknowledgements

This work was supported by the National Natural Science Foundation of China (21236003, 21206042, 20925621, and 21176083), the Basic Research Program of Shanghai (13NM1400700, 13NM1400701), the Fundamental Research Funds for the Central Universities.

Notes and references

^a Key Laboratory for Ultrafine Materials of Ministry of Education, School of Materials Science and Engineering, East China University of Science and Technology, 130 Meilong Road, Shanghai 200237, China. Fax: +86 21 64250624; Tel: +86 21 64252022; Email: yhzhu@ecust.edu.cn (Y. Zhu).

^b School of Materials Science and Engineering, East China University of Science and Technology, 130 Meilong Road, Shanghai 200237, China.

Email: jiandingchen@ecust.edu.cn (J. Chen).

† Electronic Supplementary Information (ESI) available: Detailed and additional Figures as noted in the text. See DOI: 10.1039/b000000x/

1. Y. Liang, Y. Li, H. Wang, J. Zhou, J. Wang, T. Regier and H. Dai, *Nat. Mater.*, 2011, **10**, 780-786.
2. Y. Tan, C. Xu, G. Chen, X. Fang, N. Zheng and Q. Xie, *Adv. Funct. Mater.*, 2012, **22**, 4584-4591.
3. D. Wang, H. L. Xin, R. Hovden, H. Wang, Y. Yu, D. A. Muller, F. J. DiSalvo and H. D. Abruña, *Nat. Mater.*, 2013, **12**, 81-87.
4. K. Gong, F. Du, Z. Xia, M. Durstock and L. Dai, *Science*, 2009, **323**, 760-764.
5. D. Geng, Y. Chen, Y. Chen, Y. Li, R. Li, X. Sun, S. Ye and S. Knights, *Energy Environ. Sci.*, 2011, **4**, 760-764.
6. S. Shanmugam and T. Osaka, *Chem. Commun.*, 2011, **47**, 4463-4465.
7. J. Liang, Y. Jiao, M. Jaroniec and S. Z. Qiao, *Angew. Chem. Int. Ed.*, 2012, **51**, 11496-11500.

8. R. Liu, D. Wu, X. Feng and K. Müllen, *Angew. Chem. Int. Ed.*, 2010, **49**, 2565-2569.
9. L. Lai, J. R. Potts, D. Zhan, L. Wang, C. K. Poh, C. Tang, H. Gong, Z. Shen, J. Lin and R. S. Ruoff, *Energy Environ. Sci.*, 2012, **5**, 7936-7942.
10. P. Wang, Z. Wang, L. Jia and Z. Xiao, *Phys. Chem. Chem. Phys.*, 2009, **11**, 2730-2740.
11. H. Kim, K. Lee, S. I. Woo and Y. Jung, *Phys. Chem. Chem. Phys.*, 2011, **13**, 17505-17510.
12. F. Cheng, Y. Su, J. Liang, Z. Tao and J. Chen, *Chem. Mater.*, 2009, **22**, 898-905.
13. F. Cheng, Y. Su, J. Liang, Z. Tao and J. Chen, *Chem. Mater.*, 2009, **22**, 898-905.
14. Y. Ye, L. Kuai and B. Geng, *J. Mater. Chem.*, 2012, **22**, 19132-19138.
15. X.-Y. Yan, X.-L. Tong, Y.-F. Zhang, X.-D. Han, Y.-Y. Wang, G.-Q. Jin, Y. Qin and X.-Y. Guo, *Chem. Commun.*, 2012, **48**, 1892-1894.
16. J. Liu, L. Jiang, Q. Tang, B. Zhang, D. S. Su, S. Wang and G. Sun, *ChemSusChem*, 2012, **5**, 2315-2318.
17. J.-S. Lee, G. S. Park, H. I. Lee, S. T. Kim, R. Cao, M. Liu and J. Cho, *Nano Lett.*, 2011, **11**, 5362-5366.
18. Y. Liang, H. Wang, P. Diao, W. Chang, G. Hong, Y. Li, M. Gong, L. Xie, J. Zhou, J. Wang, T. Z. Regier, F. Wei and H. Dai, *J. Am. Chem. Soc.*, 2012, **134**, 15849-15857.
19. Z.-S. Wu, S. Yang, Y. Sun, K. Parvez, X. Feng and K. Müllen, *J. Am. Chem. Soc.*, 2012, **134**, 9082-9085.
20. J. Duan, Y. Zheng, S. Chen, Y. Tang, M. Jaroniec and S. Qiao, *Chem. Commun.*, 2013, **49**, 7705-7707.
21. L.-S. Zhang, X.-Q. Liang, W.-G. Song and Z.-Y. Wu, *Phys. Chem. Chem. Phys.*, 2010, **12**, 12055-12059.
22. A. Yan, X. Liu, G. Qiu, H. Wu, R. Yi, N. Zhang and J. Xu, *J. Alloys Compd.*, 2008, **458**, 487-491.
23. U. A. Paulus, T. J. Schmidt, H. A. Gasteiger and R. J. Behm, *J. Electroanal. Chem.*, 2001, **495**, 134-145.
24. U. Johanson, M. Marandi, T. Tamm and J. Tamm, *Electrochim. Acta*, 2005, **50**, 1523-1528.
25. S. Li, Y. Qiu and X. Guo, *J. Appl. Polym. Sci.*, 2009, **114**, 2307-2314.
26. X. Zhang, S. Wang, S. Lu, J. Su and T. He, *J. Power Sources*, 2014, **246**, 491-498.
27. X. Meng, H. Cui, J. Dong, J. Zheng, Y. Zhu, Z. Wang, J. Zhang, S. Jia, J. Zhao and Z. Zhu, *J. Mater. Chem. A*, 2013, **1**, 9469-9476.
28. S. Ni, D. He, X. Yang and T. Li, *J. Alloys Compd.*, 2011, **509**, L305-L307.
29. H. Jiang, Y. Su, Y. Zhu, J. Shen, X. Yang, Q. Feng and C. Li, *J. Mater. Chem. A*, 2013, **1**, 12074-12081.
30. H.-W. Liang, W. Wei, Z.-S. Wu, X. Feng and K. Müllen, *J. Am. Chem. Soc.*, 2013, **135**, 16002-16005.
31. W. Yang, T.-P. Fellinger and M. Antonietti, *J. Am. Chem. Soc.*, 2010, **133**, 206-209.
32. B. Zheng, J. Wang, F.-B. Wang and X.-H. Xia, *Electrochem. Commun.*, 2013, **28**, 24-26.
33. H. Niwa, K. Horiba, Y. Harada, M. Oshima, T. Ikeda, K. Terakura, J.-i. Ozaki and S. Miyata, *J. Power Sources*, 2009, **187**, 93-97.
34. G. Faubert, R. Côté, J. P. Dodelet, M. Lefèvre and P. Bertrand, *Electrochim. Acta*, 1999, **44**, 2589-2603.
35. Y. Chang, F. Hong, C. He, Q. Zhang and J. Liu, *Adv. Mater.*, 2013, **25**, 4794-4799.
36. H. Peng, Z. Mo, S. Liao, H. Liang, L. Yang, F. Luo, H. Song, Y. Zhong, B. Zhang, *Sci. Rep.*, 2013, **3**.
37. Z. Li, H. Chen, H. Bao and M. Gao, *Chem. Mater.*, 2004, **16**, 1391-1393.
38. P. Mills and J. L. Sullivan, *J. Phys. D: Appl. Phys.*, 1983, **16**, 723-732.
39. P. Marcus and J. M. Grimal, *Corros. Sci.*, 1992, **33**, 805-814.
40. V. Datsyuk, M. Kalyva, K. Papagelis, J. Parthenios, D. Tasis, A. Siokou, I. Kallitsis and C. Galiotis, *Carbon*, 2008, **46**, 833-840.
41. I.-Y. Jeon, S. Zhang, L. Zhang, H.-J. Choi, J.-M. Seo, Z. Xia, L. Dai and J.-B. Baek, *Adv. Mater.*, 2013, **25**, 6138-6145.
42. K. Ai, Y. Liu, C. Ruan, L. Lu and G. M. Lu, *Adv. Mater.*, 2013, **25**, 998-1003.

-
43. D. Yu, L. Wei, W. Jiang, H. Wang, B. Sun, Q. Zhang, K. Goh, R. Si and Y. Chen, *Nanoscale*, 2013, **5**, 3457-3464.